Data-Driven Design Space Analysis for Multi-Material Thermoplastic Composites Manufactured by Fused Filament Fabrication

Seda Oturak[1,2], Melinda McKeehan[1], Callie Zawaski[3], and Wesley F Reinhart[1,2]

[1]Department of Materials Science and Engineering, The Pennsylvania State University, University Park, PA, USA
[2]Institute for Computational and Data Sciences, The Pennsylvania State University, University Park, PA, USA
[3]Applied Research Laboratory, The Pennsylvania State University, University Park, PA, USA

Corresponding author:
Wesley F Reinhart, The Pennsylvania State University, Steidle Building, University Park, PA, 16802, USA
Email: reinhart@psu.edu

Abstract

Multi-material additive manufacturing has enabled the fabrication of components with highly tailored mechanical responses. However, as both manufacturing processes and constituent materials become more sophisticated, the large number of process variables makes design increasingly challenging. Here, we investigate the design space for multi-material thermoplastic composites produced by a commercially available fused filament fabrication printer. We consider the uniaxial compression of neat materials with sample geometry and toolpath variations, as well as composites comprised of a soft elastic matrix with stiff reinforcement material in different reinforcement fractions and geometries. We find that some changes to the toolpath can have a significant impact on the compressive behavior of the samples due to the high anisotropy of the filaments. The composite geometries were found to exhibit different specific strengths relative to reinforcement fraction, and their compressive behavior matched qualitatively but not quantitatively to predictions from finite element analysis. To understand the performance space, we analyzed the experimental dataset with truncated Singular Value Decomposition. Surprisingly, despite the complexity of the system, 97.8% of the variance in stress-strain curves of our samples was captured by the first component and 99.9% by the first two. The shape of the components indicates that while the stress-strain curves of samples may vary quantitatively, very limited modes are controllable with the design variables considered here. In effect, the strength of the composite could be controlled by manipulating reinforcement mass fraction, but the shape of the nonlinear behavior was largely baked into the constituent materials despite changing the reinforcement geometry. This result has important consequences that must be considered early in the design process when developing new multi-material systems to achieve tailored mechanical responses.

Keywords

additive manufacturing, compression, thermoplastic composites, design space exploration

Introduction

Additive manufacturing (AM) has enabled the rapid manufacturing of personalized designs for ergonomic improvements in comfort, performance, and cost. This can be seen in applications such as personalized prosthetics,[1] braces,[2] athletic wear,[3] and footwear.[4] The unique geometries of each individual can be measured in 3D to capture the individual's shape and print form-fit parts.[5] Most of these applications include the requirement for not just a geometric fit but also prescribed behavior under compressive loading. This revolution has been made possible by advances in both computational design and precision in the additive manufacturing processes.

Material response, such as compliance behavior, can be increasingly tailored by spatially varying geometry throughout a part. For example, compression behavior can be tuned for anisotropic behavior[6] or a honeycomb structure can be tailored by altering the wall thickness and depth for energy absorption across a part.[7] By expanding the design space to include multiple materials, such as those with different elastic moduli, the achievable design space is further broadened.[8] Spatially varying multi-material designs can thus achieve performance that is unobtainable using a single material structure and provide new opportunities for functionally graded parts.[9,10]

Printed thermoplastic polyurethane (TPU) allows for the AM fabrication of complex geometry for impact[13] and compression.[14,15] Its tensile behavior in fused filament fabricated (FFF) parts has been studied extensively.[16,17] With the right chemistry, even dissimilar polymers can bond during the FFF printing process.[18,19] Consequently, many multi-material parts have leveraged TPU for its flexibility in conjunction with other, stiffer materials.[20–22] This existing literature provides a convincing picture of TPU's utility in FFF, as it can be readily printed, is compatible with other polymer filaments, and is more flexible than other materials such as polylactic acid (PLA) or acrylonitrile butadiene (ABS). However, little work has been conducted on compressive behavior of FFF printed TPUs,[23,24] and even less on TPU composites produced by multi-material FFF; to our knowledge, only one study on compressive behavior of FFF TPU/TPU composites exists in the literature.[25]

Optimization of AM during part manufacturing is a challenging task due to the vast space of process variables.[26] This has led to increased interest in data science methods to analyze experimental observations and design new materials or processing routes.[27] Linear projection schemes such as Principal Component Analysis (PCA) or the closely related Singular Value Decomposition (SVD) are commonly used for dimensionality reduction when modeling and visualizing high dimensional data.[28,29] For instance, PCA has been used for visualizing the design space in many engineering problems, such as understanding the process-structure relationships in AM,[30] predicting the cohesive energy of compounds,[29] and understanding the effects of shape and other physical factors on airfoil design[31–33] and turbine blades.[34] These strategies allow for more human-friendly visualizations of high-dimensional data, facilitating understanding of complex design spaces.

In this work, two different grades of TPU with highly contrasting mechanical properties were integrated into solid multi-material composite parts to understand the effects of the structural and process parameters on the material performance under compressive loading. Relatively few studies have been published on the compressive behavior of TPU in either single- or multi-material FFF components, and very few on the compressive behavior of TPU/TPU composites in general. In our study, the components are reinforced by two different patterns with varying geometric features that span a wide range of reinforcement ratios. The patterns were fabricated on a commercially available 3D printer, and their mechanical strength was evaluated. The stress-strain curves representing the mechanical behavior of the parts were analyzed by SVD in an effort to quantitatively describe the complexity of the materials and fabrication process.

Materials and Methods

Materials

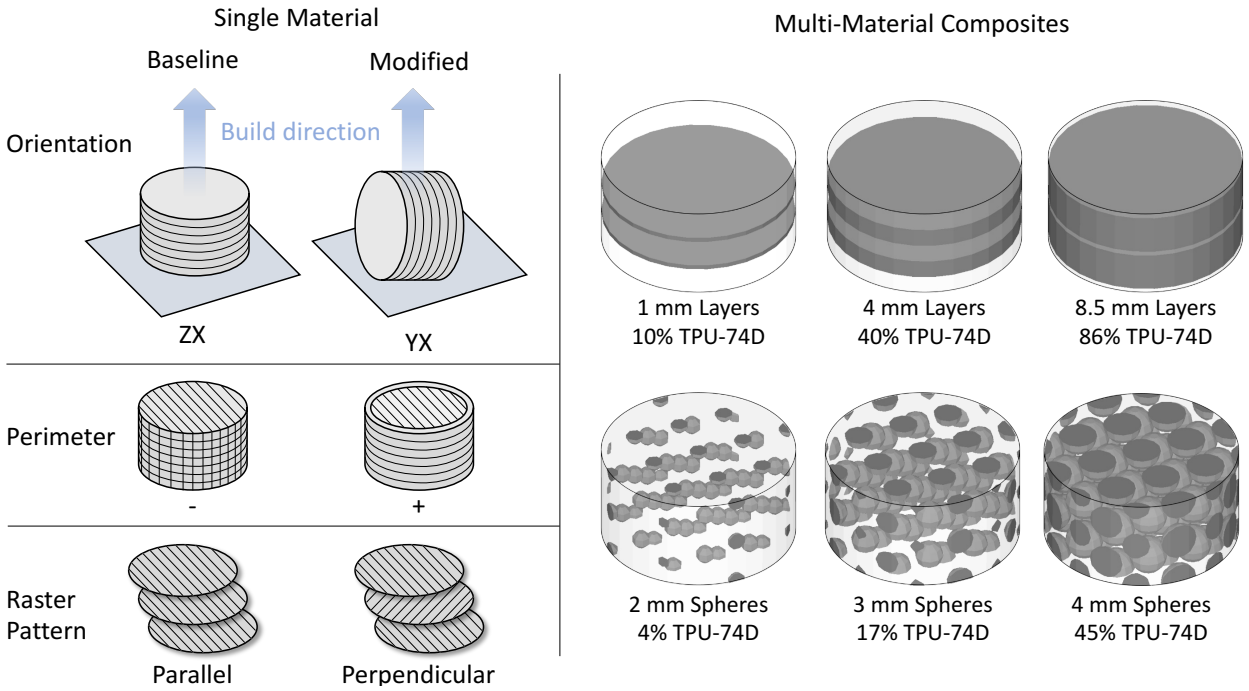

Figure 1. Schematic representation of the variations to sample geometry and toolpath considered in this study. For single material designs, we varied build orientation, perimeter ring, and raster pattern as shown. For multi-material composites, we investigated layers and spherical inclusions of reinforcement material. TPU-80A is represented in the renderings as translucent and TPU-74D is represented as dark gray, corresponding to their physical appearance.

Table 1. Material properties from the manufacturer are based on the neat, unprinted material, and the tensile modulus and elongation are based on manufacturer-printed parts.[37,38] Orientations used in this study are illustrated in (Figure 1).

Identifier	TPU-80A			TPU-74D		
Name	Essentium TPU 80A LF			Essentium TPU 74D		
Shore Hardness	80A			73D		
Specific Gravity	1.11 g/cm3			1.23 g/cm3		
Build Direction	XY	YX	ZX	XY	YX	ZX
Tensile Modulus (MPa)	22	18	17	340	314	316
Elongation at break, %	640	517	471	730	73	110

Thermoplastic polyurethane (TPU) was selected as the most elastic printable material available because it can be produced with vastly different hardness. By selecting two different TPU materials rather than two distinct polymers, it is less likely to run into miscibility issues in bonding. Materials were purchased from Essentium in filament form with a diameter of 2.85 mm. Some selected properties of the two materials are outlined in (Table 1). Most importantly, the two grades of TPU have vastly different hardness, with TPU-80A having a Shore hardness of 80A and TPU-74D having a Shore hardness of 73D. The difference between these materials is also shown by tensile modulus varying by more than 15x (varying slightly in different directions).

Note that the orientations described in this text refer to the build orientation rather than solid mechanics notation; all mechanical behaviors in this work are uniaxial compressive loading. The XY

build orientation refers to a flat tensile bar with printed roads aligned in the load direction, YX refers to a flat tensile bar with printed roads aligned perpendicular to the load direction, and ZX refers to a vertically printed tensile bar. Our typical load case best resembles ZX but in compression. We also perform limited tests of the YX case. See (Figure 1) for a schematic representation of these directions.

Material was dried in a vacuum oven at 70 °C for a minimum of 8 hours and stored in closed air-tight containers to minimize variation in the material due to moisture content.[35,36] While printing, the material was stored in a dry box (PolyBox edition II). The material was redried as needed when the material exhibited observable bubbles while printing. Note that we did not verify these tensile properties independently; we only performed compression tests in this study.

Sample design and fabrication

A variety of disk-shaped specimens with a 40 mm diameter and 20 mm height were designed for compression testing. Neat samples of TPU-80A and TPU-74D were prepared in addition to composites with one of two basic reinforcement geometries, which are shown in (Figure 1). The first composite design was a quasi-1D pattern (i.e., varying only in the build axis) consisting of printed layers with uniform thickness within each sample. Overall sample geometry remained constant, while the amount of reinforcing TPU-74D within the TPU-80A matrix varied. Thus, the single design variable for layered composites was the reinforcement layer thickness. The second composite design used a body-centered cubic lattice of spherical inclusions, with a lattice site in the center of the sample's bottom face (since spheres are centered at lattice sites, the spheres on the bottom are only half-spheres). The distance between the centers of neighboring spheres was held constant at 10 mm while the radius of the spheres varied. Thus, the single design variable for the spherical reinforcement was the diameter of spherical inclusions.

Table 2. Selected printing parameters are used in the Cura slicer to generate printer gcode.

Nozzle diameter	0.5 mm	
Layer height	0.4 mm	
Bed temperature	45 °C	
Print speed	750 mm/min	
	TPU-80A	TPU-74D
Nozzle temperature	225 °C	235 °C

Sample fabrication was performed on a Lulzbot Taz Pro with dual-head extrusion. Toolpaths were generated using the Cura (Lulzbot Cura SteamEngine 3.6.23). Some relevant printing parameters used to generate toolpaths for the fabricated samples are shown in (Table 2). All samples used fully dense designs (i.e., 100% infill) and were printed flat on the print bed with aligned infill and material retraction off. Perimeters were turned off unless otherwise specified. When they were used, three layers were used for walls (so the use of a perimeter implies three concentric filament rings throughout this study). Renderings of the actual toolpaths used in this study are available in SI for selected geometries.

Both TPU materials were challenging to print with FFF, requiring extensive process tuning to achieve reliable prints. A raft was required to overcome poor bed adhesion in TPU-74D. A purge tower was employed to assist in switching between filaments in the multi-material geometries. Lastly, the flexibility of the TPU materials resulted in under-extrusion caused by the material buckling when compressed into the nozzle, slipping on the extruder gear, material degradation restricting material flow over time, and stretching as it was pulled from the filament spool. An extrusion multiplier was added to help compensate for the under-extrusion of the material; however, due to inconsistencies in the material flow restriction, some under-extrusion was still observed, specifically in the highly elastic

TPU-80A. Note that this leads to samples that are not fully dense despite using 100% infill in the design.

Overall, we include data from 74 samples representing 18 different designs and/or process parameters. This is an average of 4 samples per design, but the mode is 3, with a minimum of 1 and a maximum of 14; the exact number of replica samples for each design is given in the SI. In short, we decided to fabricate more replicas of some designs due to high variability in the fabrication process, and for the case of the single replica (the only case with less than 3), we could only fabricate one suitable sample due to the challenges with printing TPU-80A.

Uniaxial compression testing

An Instron 8511 servo-hydraulic test frame operated by an Instron 8800 controller and equipped with a 20 kN actuator and 22 kN load cell was used for compression testing the printed samples. The specimens were centrally positioned between two flat platens and loaded in position control at a rate of 1 cm/min. The compression tests were performed by loading and unloading in a single run, with cyclic loading repeated three times during the compression test for each sample. Force-displacement curves were obtained for each sample, which were converted to engineering stress and engineering strain based on the nominal cross-section and height. We will refer to these post-processed data (i.e., paired engineering stress and engineering strain) as stress-strain curves.

Data preparation

We applied a preloading of 0.2 MPa to account for compliance at the start of compression; this accounts for at most 2% of the maximum stress and as little as 0.8%. To compute statistics, we resampled the strain data at the same stress values using linear interpolation. Mean and standard deviation were thus computed on strain data for a given stress across multiple samples.

Finite Element Analysis

Finite Element Analysis was performed using FeNICS, an open-source solver.[39,40] Tetrahedral meshes were generated using gmsh.[41] Following relevant literature,[42,43] the constitutive model was a compressible Yeoh hyperelastic model with the following form:[44]

$$W = \sum_{i=1}^{3} C_{i0}(\bar{I}_1 - 3)^i + \frac{\kappa}{2}(J-1)^2,$$

where W is the strain energy, J is the volume ratio, I_1 is the first invariant of the Cauchy-Green strain tensor, and C_i and κ are empirical parameters to be fitted. Dirichlet boundary conditions were applied at the top and bottom surface of the cylindrical sample, with nodes at the bottom surface Γ_B fixed to $\boldsymbol{u} = 0$ and nodes at the top surface Γ_T fixed to $\boldsymbol{u} = (0, 0, -\delta)$ where δ is the fixed displacement to enforce a target strain. This δ was then gradually increased using the preceding $\boldsymbol{u}$ as an initial guess. The reaction force R_z was obtained by integrating $\sigma_{zz}(\boldsymbol{u})$ over the surface Γ_T.

Two separate material models were obtained by fitting to experimental data for the neat TPU-74 and TPU-80 samples with 40 mm diameter. Fitting was performed using Bayesian Optimization with the open-source dragonfly package.[45] The best-fitting model parameters were:

$$\theta_{TPU-74}: \{C_{10} = 16.839\ \text{MPa}, C_{20} = 24.458\ \text{GPa}, C_{30} = 109.74\ \text{MPa}, \kappa = 48.226\ \text{MPa}\}$$
$$\theta_{TPU-80}: \{C_{10} = 0.81818\ \text{MPa}, C_{20} = -1.0000\ \text{MPa}, C_{30} = 7.7778\ \text{MPa}, \kappa = 6.0000\ \text{MPa}\}$$

These material parameters were then applied to simulations of the composite geometries.

Dimensionality reduction

Truncated SVD is a dimensionality reduction technique by which the original, high-dimensional data are projected onto a linear basis set. The basis set is truncated to include only the components with the top-*k* greatest eigenvalues to effectively reduce the dimensionality of the data. Since the limiting factor in our compression experiments was the maximum force of our load cell, we chose to consider strain values at fixed stress. We, therefore, interpolated the strain data from each sample at fixed stress values between zero and the minimum maximum strain across all the samples (9.16 MPa) for consistency. The SVD was then performed on these vectors of resampled strain values, with every test specimen having data at each of the given stress values. SVD was performed using scikit-learn.[46]

Results and discussion

Neat samples

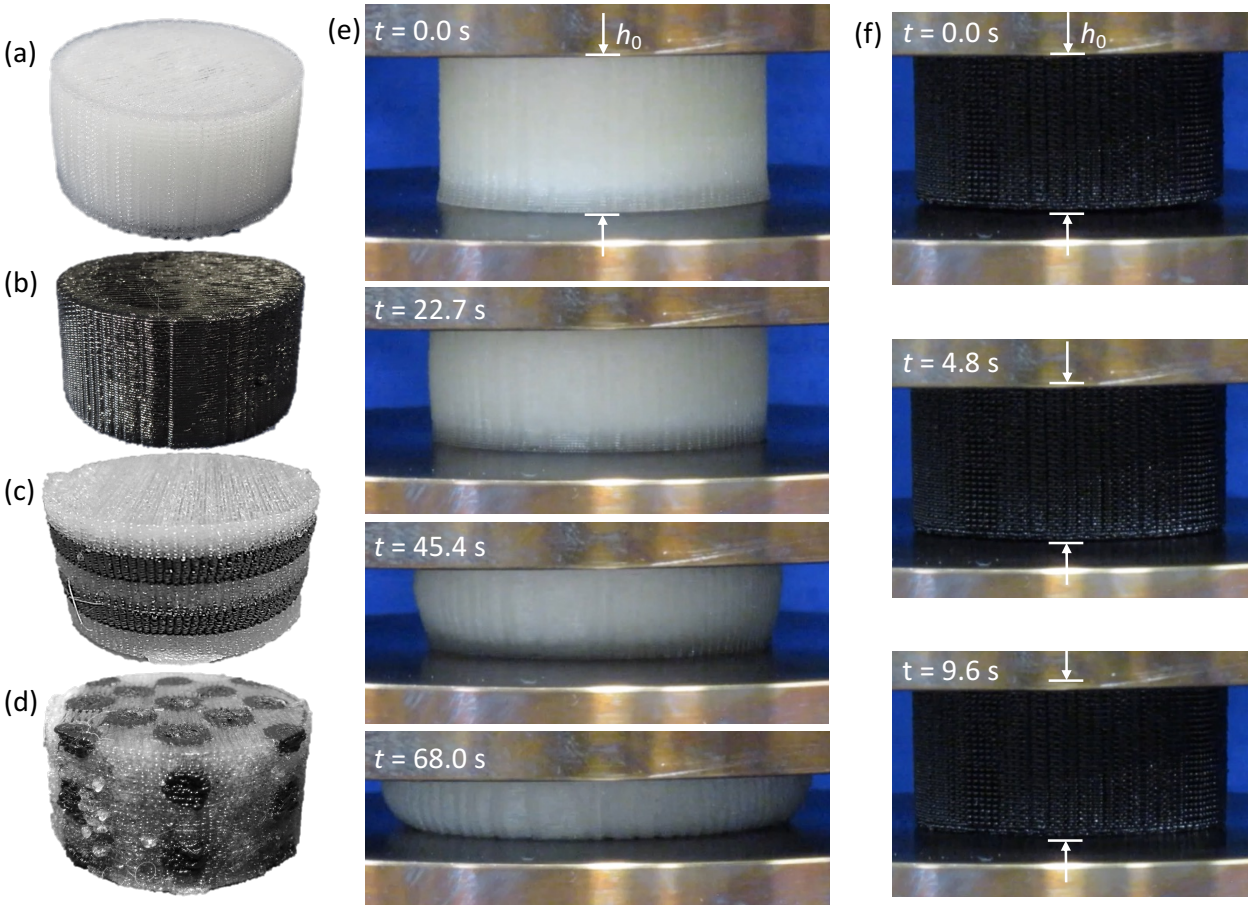

Figure 2. Images of experimental samples produced by FFF: (a) neat sample of TPU-80A, (b) neat sample of TPU-74D, (c) composite sample with layered reinforcement, (d) composite sample with spherical inclusions. Images taken during the compression of neat samples of (e) TPU-80A and (f) TPU-74D at different times, *t*. The initial height of the sample h_0 is indicated by white bars since the final displacement is relatively small in the case of TPU-74D.

Cyclic loading was applied to samples of each neat material with 40 mm diameter and standard print settings. Hysteresis was observed between the first and second cycles, with the softer TPU-80A exhibiting hardening, likely due to densification, while the stiffer TPU-74D exhibited slight softening

behavior. Only minimal hysteresis was observed in subsequent loading cycles, so the analysis in the remainder of this study considered only the loading part of the second cycle. Some sample load-unload curves are shown in the SI.

Using this protocol, we evaluated the effect of different geometries and toolpaths on the mechanical properties of neat samples. The first set are neat samples with different diameters (30 mm, 40 mm, and 50 mm), while the rest are all nominally the same geometry (40 mm diameter and 20 mm height) and the same processing parameters as given in (Table 2). However, we explored the effect of different raster patterns during infill, different build orientations, and the use of perimeter rings (◯). The influence of toolpath will need to be considered when designing composite geometries since it is impossible to utilize the same toolpath for all composite designs.

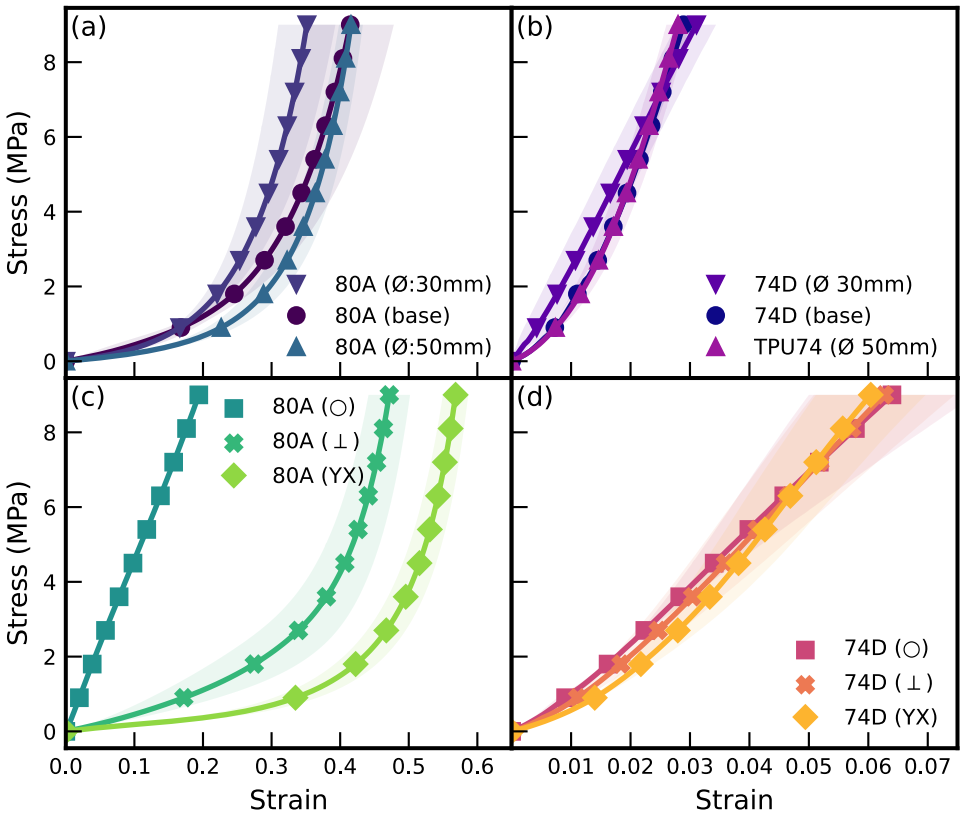

Figure 3. Compression test results for neat samples. (a) TPU-80A samples and (b) TPU-74D samples with different diameters but otherwise identical slicer settings. (c) TPU-80A and (d) TPU-74D samples with different slicer settings as indicated in (Figure 1): perimeter ring, perpendicular raster pattern, and YX build orientation. Data in all panels have been resampled at equivalent stress as described in methods and truncated to the highest common stress.

The effects of different geometries and toolpaths are shown in (Figure 3). Compression data were analyzed for different sample diameters for neat materials in panels a-b. In short, the effect of the sample diameter (⌀) on compressive behavior was minimal (within uncertainty bands). Toolpath variations are shown in (Figure 3)c-d. For TPU-80A, both the perpendicular raster pattern (⊥) and YX build orientation resulted in slightly reduced stiffness compared to baseline, while the perimeter rings resulted in increased stiffness. For TPU-74D, the differences between the toolpaths were insignificant. We conclude that under-extrusion of TPU-80A leads to greater discrepancy in the densification behaviors with different toolpaths, while the easier-to-print TPU-74D shows less deviation.

Among these experiments, the most significant effect was observed by adding perimeter rings for the TPU-80A samples. We expected this to change the densification behavior as the material will be stronger in tension along the filament compared to the bonding between filaments. We suspect that the perimeter rings reduce cross-section expansion during compression. Therefore, this may be an artifact of using engineering stress instead of true stress.

Composite samples

Next, we introduce multi-material composite samples. Each composite sample has a diameter of 40 mm and a height of 20 mm, and the slicer settings were fixed throughout, with a “parallel” raster pattern and no perimeter rings. Increasing the amount of TPU-74D reinforcement material should increase the overall strength of the composite compared to neat TPU-80A, eventually approaching the strength of neat TPU-74D. Here, we seek to establish the degree to which the behavior of the composite can be controlled independently of this reinforcement fraction by manipulating reinforcement geometry.

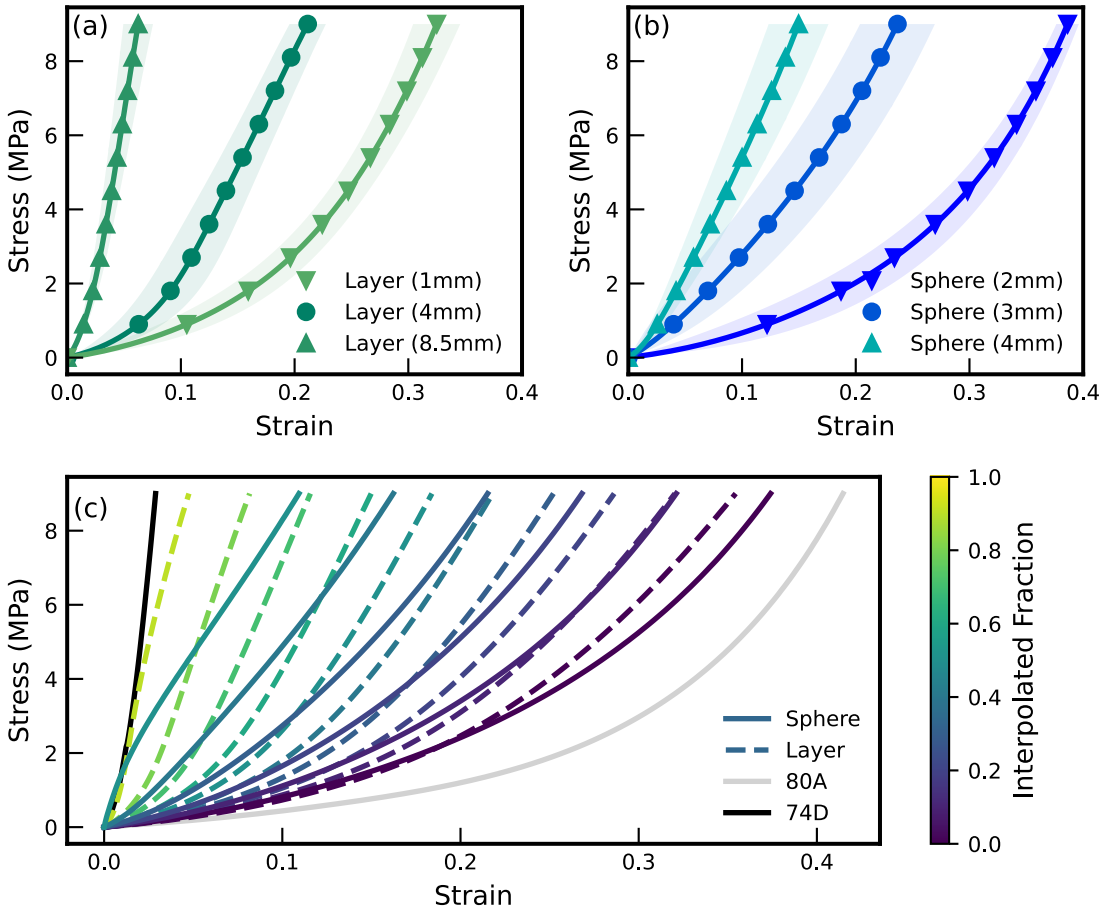

Figure 4. Compression test results for composite samples with different reinforcement geometries. (a) Layered reinforcements and (b) spherical reinforcements on a lattice. Data have been resampled and truncated to common stress values as described above. (c) Linear interpolation of different reinforcement styles over the full range of reinforcement volume fraction. Spheres are only shown to 60% as they become nonsensical at high volume fraction.

For composite samples with layered reinforcements, the layer thickness of TPU-74D was manipulated while keeping a constant number and arrangement of layers. The reinforcement fraction for spheres was manipulated by varying the radius of inclusions. The resulting compression data are

shown in (Figure 4) for each reinforcement type. In the weakest cases, the samples exhibit a shallow slope before densification, similar to the neat TPU-80A samples, while the strongest cases exhibit a steeper slope that is also more linear, similar to the neat TPU-74D samples. The middle cases exhibit a blend of these behaviors, as expected.

To compare the observed compression behavior between the two reinforcement types, it is necessary to consider the reinforcement volume fraction, as reported in (Figure 1). Note that the layer reinforcement designs have roughly twice the reinforcement material in each sample compared to the sphere reinforcements. This necessitates a more detailed comparison that considers (nearly) equivalent volume fractions of the reinforcement material. We probe these differences between reinforcement geometries in (Figure 4c), which shows the sphere reinforcement, layer reinforcement, and neat samples interpolated to many different volume fractions.

At moderate volume fractions, sphere reinforcements provide a higher slope at low strain but grow to a lower slope at high strain compared to the layer reinforcements. This can be seen in the 50% curve for spheres (second to last, teal-blue color), whose stress grows faster than the 50% curve for layers but ultimately approaches a similar value at around 15% strain. Both reinforcement types outpace the expected behavior obtained by interpolating from neat samples, reaching neat TPU-74D well ahead of 100% interpolated volume fraction. The shape of these curves is due to the different compaction behavior of spherical inclusions compared to horizontal layers of TPU-74D in the composites. Spheres on a lattice will span the sample in the load axis faster than the layer samples, providing greater stiffness at lower strain. Meanwhile, the stiffness of the TPU-74D in the layer reinforcements will not become relevant until the compliant TPU-80A begins to densify, at which point the TPU-74D will start to dominate the response.

Finite Element Analysis

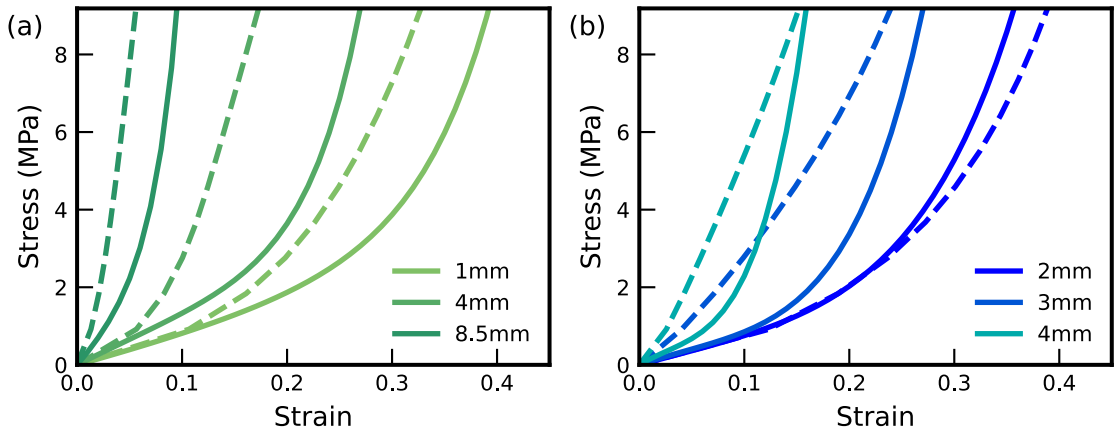

Figure 5. Result of the FEA on composite geometries for (a) layer geometries and (b) sphere geometries. Solid lines are the simulation results while dashed lines are experimental data reproduced from (Figure 4).

Calibrated constitutive models were obtained for each of the neat TPU materials as described in the (Materials and Methods). The calibrated models were deployed to simulate the performance of the composites shown in the preceding sections. The results in (Figure 5) show that the model successfully captures the qualitative behavior of the composites (e.g., approximate ratios of strength between different geometries) but does not quantitatively match the experimental results. In particular, the experimental composite samples were stiffer than the models would suggest. The discrepancy is likely due to the strong influence of the toolpath, which has not been included in the continuum simulation model; it is fundamentally impossible to achieve an identical toolpath when fabricating

samples with different reinforcement geometries (i.e., one toolpath cannot fabricate spheres of different radii).

To be clear, our FEA model treats the bonded filaments as a single continuous body with isotropic properties. With FFF, this is not the case, as bonded filaments will result in a highly anisotropic material that fails first at interfaces between filaments (such as between layers). In our analysis, we are considering the continuum results to be descriptive of the effect of reinforcement geometry, while interfaces between filaments and between layers are intrinsically tied to the toolpath. Thus, when we say the discrepancy is related to the toolpath, we mean that the discrepancy between the FEA results and the experimental results is indicative of the bonding interfaces that have not been included in the FEA model. We chose this simplified FEA approach as a first step to isolate the effects of reinforcement geometry.

The best example of the discrepancy is the 4 mm sphere geometry, where the simulated behavior is much more compliant at low strain compared to the experiment. The 2 mm sphere geometry gives the best match, which also corresponds to the smallest reinforcement volume fraction. Meanwhile, all the layered geometries in (Figure 5a) show poor agreement between the simulation and experiment, but by a consistent margin. This inconsistency between the two reinforcement styles is further evidence of the influence of the toolpath, as each build slice in the layer designs has the same toolpath no matter the reinforcement thickness, while the sphere designs have toolpaths in each slice that depend on the size of the spheres.

Dimensionality reduction

The objective of this study is to probe the degree to which the compressive behavior of fully dense thermoplastic composites can be tuned by adjusting reinforcement geometry. In examining the many variations of similar compression curves above by eye, the answer to this question remains unclear; though the overall strength of different samples varies, they all exhibit a similar nonlinear behavior that is difficult to tell apart. We now seek to address this question via a data-driven approach, namely, the application truncated SVD to all the stress-strain curves.

The number of dimensions to retain in truncated SVD projection can be determined by evaluating the explained variance ratio. In essence, each vector component of the right singular matrix captures a certain amount of overall variance in the data when it is used in the projection. In our SVD, the first component captured 97.8% of the total variance in strain data, while the second component captured an additional 2.1%. In other words, we can represent 99.9% of the total variance in the strain curves (interpolated to consistent, fixed stress values) by linearly projecting onto only the first two vector components of the SVD shown in (Figure 6).

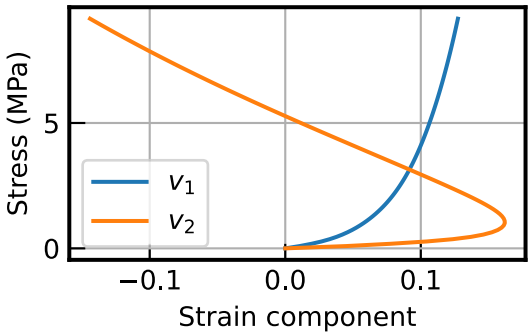

Figure 6. First and second components from SVD on the resampled experimental stress data.

The two-dimensional design space obtained from truncated SVD enables us to understand how the reinforcement geometry, reinforcement volume fraction, and toolpath affect the mechanical response of the fabricated samples. The embedding of all samples into this space is shown in (**Error! Reference source not found.**a). First, we observe that the TPU-74D and TPU-80A define opposite ends of the primary vector component, v_1. From its shape in (Figure 6), we think of v_1 as a proxy for strength, as it captures more than 98% of the variance in the compression data and closely resembles the shape of each stress-strain curve. Within this landscape, there is a cloud of data with different strengths because of different reinforcement geometry and toolpaths.

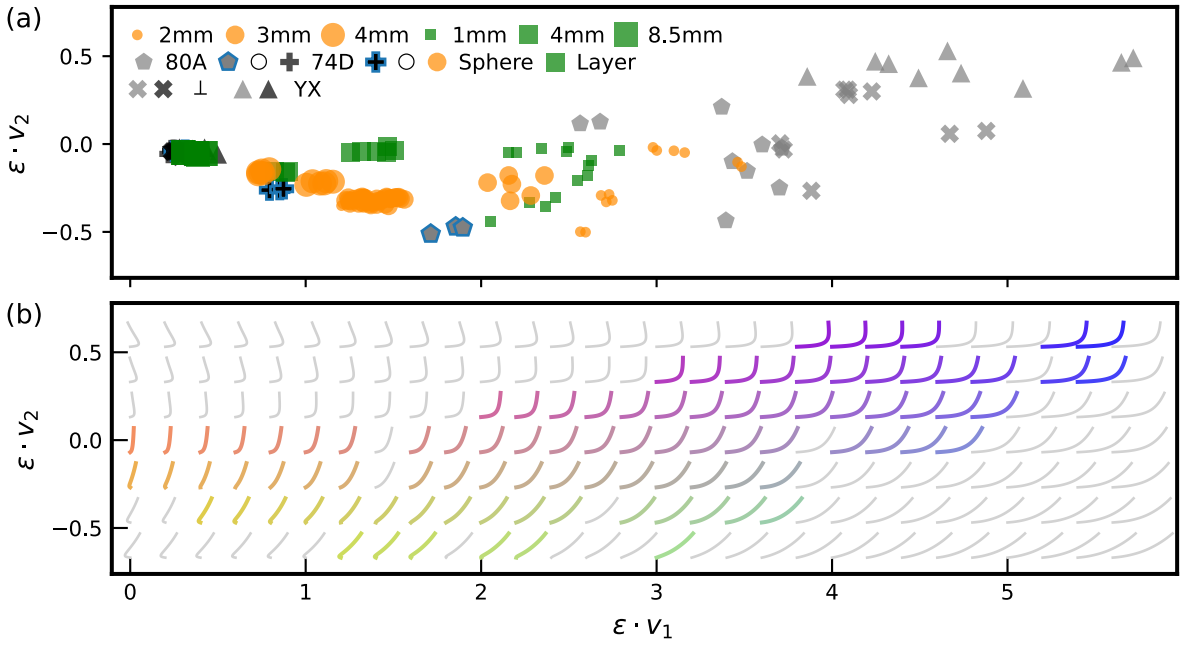

Figure 7. (a) Projection of the experimental stress-strain curves into 2D space using truncated SVD depicts the distribution of the samples having different structural properties and processing histories. (b) Reconstructed stress-strain curves embedded in-place into the low-dimensional SVD space. Each curve is a linear reconstruction from the 2D coordinates at its center. Grey curves have a Euclidean distance greater than 0.20 away from the nearest experimental data point, while the rest are colored according to a 2D Steiger colormap.

Next, we investigate the second component, v_2. This component explains less than 2% of the overall variance in the stress-strain curves and is associated with greater compliance at low strain; positive v_2 accentuates the nonlinearity inherent in low strain from v_1, while negative v_2 counteracts it and results in less initial compliance (more linear). A good example of the difference between high and low v_2 is the addition of perimeters to neat TPU-74D samples, which reduces the v_2 component and is shown in (Figure 3) to increase the linearity of the compressive behavior without greatly affecting the overall strength.

The experimental data define a shallow arc through the design space. We visualize this through reconstructions of the stress-strain curves on a grid in SVD space, shown in (**Error! Reference source not found.**b). Colored curves appear near to at least one experimental curve, while grey curves are in the unphysical region. From this visualization, it becomes clear that some regions have shapes that are not permitted by the physics of uniaxial compression, while others are feasible but aren't represented in the experimental data. New reinforcement geometries might be able to access these regions.

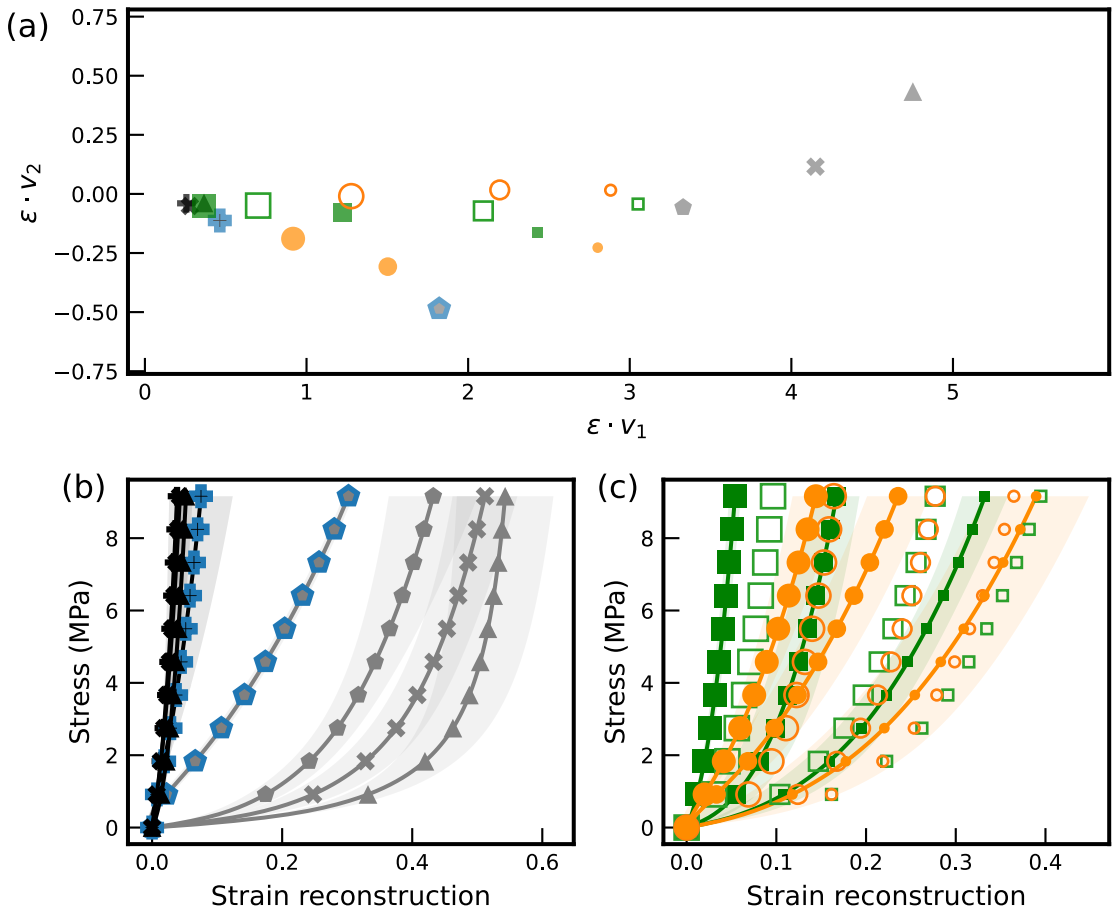

Figure 8. (a) Centroids of each group of samples in the low-dimensional SVD space. Experimental data are shown with filled symbols while simulation data are shown with open symbols. Note that the aspect ratio differs from (**Error! Reference source not found.**), such that the magnitudes of the eigenvalues are not depicted here. (b) Reconstructions of the full stress-strain curves from the neat samples in panel (a) with standard deviations within each sample group indicated by shaded bands. (c) Reconstructions of the full stress-strain curves from the composite samples in panel (a) with standard deviations within each sample group indicated by shaded bands. Simulation results are again shown with open symbols.

Due to the large number of samples in (**Error! Reference source not found.**), we produced another projection where each geometry was represented by the centroid of all samples with that geometry. These are shown in (**Error! Reference source not found.**a), while reconstructions of their stress-strain curves are shown in (**Error! Reference source not found.**b-c). In the v_1 direction, the extremes are defined by neat TPU-74 and TPU-80A materials; this effect can be observed in the reconstructed curves with TPU-74D appearing at the far left and TPU-80A appearing at the far right. In the v_2 direction, the extremes are defined by TPU-80A with perimeters and TPU-80A with YX build orientation. The difference can again be seen in the reconstructed curves, with TPU-80A perimeters being nearly linear even at low strain and TPU-80A YX showing the greatest compliance at the lowest strain of any geometry.

We also projected the simulated stress-strain curves from (Figure 5) onto the SVD components defined by the experimental data. Here, the simulated curves represented by open symbols in (**Error! Reference source not found.**a), appear confined to a quasi-1D curve within the 2D design space. Based on the preceding analysis, variation in the v_2 direction is almost entirely the result of toolpath variation. Thus, this confinement supports the idea that variation in the toolpath is responsible for the

poor agreement between simulation and experiment in (Figure 5). Reviewing the reconstructions in (**Error! Reference source not found.**b) shows that moving in the $-v_2$ direction leads to less compliance at low strain (i.e., more linear behavior), matching the experimental curves in (Figure 5).

Conclusion

In this study, we explored the design space of multi-material TPU/TPU composites manufactured by FFF additive manufacturing and tested under uniaxial compressive loading. We manufactured a total of 74 samples across 18 different designs comprising some with no reinforcements, spherical reinforcements, and layer reinforcements, and explored the effect of different toolpaths by including perimeter rings, alternating raster patterns, and different build orientations, with other factors held constant. Due to the non-linear behavior of the TPUs and the many variations of geometric and process variables, many stress-strain curves were obtained. Constitutive models for the TPU materials were calibrated using Bayesian Optimization, and Finite Element Analysis was performed to predict the behavior of the composites. Finally, we analyzed the experimental data using truncated SVD to elucidate the response space.

Overall, only minor effects on the compressive behavior were observed when testing different variations of neat material samples. The purpose of these tests was to establish a baseline amount of variance expected from changes to sample geometry and toolpath within a dense sample of neat material before introducing the multi-material composite parts. The one standout case was the perimeter filament rings, which resulted in stiffer, more linear compressive behavior. When considering the response space of multi-material composites, spherical inclusions provided greater strength compared to layer reinforcements of equal reinforcement fraction. This supports the observation that toolpaths with perimeter rings have a proportionally greater effect on overall compressive strength due to how tension in the perimeter filament affects densification. As a consequence, TPU FFF parts designed for compressive loading could benefit from additional perimeter walls to take advantage of the tensile strength of the filament. It is not clear from our study whether there is an optimal number of such perimeter walls or if the strongest samples would result from infill with concentric shells.

Surprisingly, despite the complexity of the system, 97.8% of the variance in stress-strain curves of our samples was captured by the first component and 99.9% by the first two. The shape of these vectors indicates that while the behavior of samples varies quantitatively, limited modes are controllable with the design variables considered here. In effect, the strength of the composite could be controlled by manipulating reinforcement mass fraction, but the shape of the nonlinear behavior was baked into the constituent materials despite changing the reinforcement geometry. This was true in both the simulations (subject only to geometrical variations) and the experimental results (subject also to significant process variation, including toolpath).

In the future, further tuning may be required to better control the extrusion rate of each material and obtain more insight into geometry-specific behaviors. From our initial results, it seems clear that nozzle diameter, layer height, and other aspects of the design will also play a role in the overall strength of the parts, but introducing these will greatly expand the scope of work and complexity of the resulting analysis. It would also be interesting to explore more complex reinforcement geometries, which will impact the mechanical response both directly through the nominal geometry as well as incidentally through the effect of the toolpath. While simulation was not successful in capturing the quantitative response of the composites, it may assist in identifying geometries to obtain more novel response modes (i.e., through data-driven design).

Acknowledgments

We thank Eric C. Strauch for assistance with the compression testing protocol.

CRediT statement

Seda Oturak: Methodology, Software, Formal analysis, Investigation, Data Curation, Writing - Original Draft, Writing – review & editing, Visualization
Melinda McKeehan: Software, Investigation, Data Curation, Writing - Original Draft
Callie Zawaski: Conceptualization, Methodology, Investigation, Writing - Original Draft, Writing – review & editing, Supervision, Project administration, Funding acquisition
Wesley Reinhart: Conceptualization, Software, Formal analysis, Visualization, Writing - Original Draft, Writing – review & editing, Supervision, Project administration, Funding acquisition

Conflict of Interest statement

The authors declare no conflict of interest.

Funding statement

This work was supported by a seed grant from the Pennsylvania State University's Materials Research Institute (MRI) and Applied Research Laboratory (ARL).

References

1. ten Kate J, Smit G, Breedveld P. 3D-Printed Upper Limb Prostheses: A Review. Disabil Rehabil Assist Technol 2017;12(3):300–314; doi: 10.1080/17483107.2016.1253117.
2. Venumbaka SA, Covarubias M, Cesaro G, et al. Application of Multi Materials Additive Manufacturing Technique in the Design and Manufacturing of Hand Orthoses. 2020; pp. 461–468; doi: 10.1007/978-3-030-58805-2_55.
3. Beiderbeck D, Krüger H, Minshall T. The Future of Additive Manufacturing in Sports. 2020; pp. 111–132; doi: 10.1007/978-3-030-50801-2_7.
4. Xie J, Zhou Z, Luo T, et al. Study on Design and Additive Manufacturing of Customized Bionic Sports Sole for the Elderly. IEEE Access 2021;9:69830–69838; doi: 10.1109/ACCESS.2021.3078162.
5. Parry EJ, Best JM, Banks CE. Three-dimensional (3D) scanning and additive manufacturing (AM) allows the fabrication of customised crutch grips. Mater Today Commun 2020;25; doi: 10.1016/j.mtcomm.2020.101225.
6. Wang P, Yang F, Lu G, et al. Anisotropic compression behaviors of bio-inspired modified body-centered cubic lattices validated by additive manufacturing. Compos B Eng 2022;234; doi: 10.1016/j.compositesb.2022.109724.
7. Kumar S, Ubaid J, Abishera R, et al. Tunable Energy Absorption Characteristics of Architected Honeycombs Enabled via Additive Manufacturing. ACS Appl Mater Interfaces 2019;11(45):42549–42560; doi: 10.1021/acsami.9b12880.
8. Yavas D, Liu Q, Zhang Z, et al. Design and fabrication of architected multi-material lattices with tunable stiffness, strength, and energy absorption. Mater Des 2022;217; doi: 10.1016/j.matdes.2022.110613.
9. Gaynor AT, Meisel NA, Williams CB, et al. Multiple-Material Topology Optimization of Compliant Mechanisms Created Via PolyJet Three-Dimensional Printing. J Manuf Sci Eng 2014;136(6); doi: 10.1115/1.4028439.
10. Zheng X, Williams C, Spadaccini CM, et al. Perspectives on multi-material additive manufacturing. J Mater Res 2021;36(18):3549–3557; doi: 10.1557/s43578-021-00388-y.

11. Rahman KM, Letcher T, Hu Z. Effects of Defects on the Performance of Hierarchical Honeycomb Metamaterials Realized Through Additive Manufacturing. In: Volume 2: Advanced Manufacturing American Society of Mechanical Engineers; 2016; doi: 10.1115/IMECE2016-66940.
12. Minguella J, Challa PR, De Los Santos MA, et al. Re-design of a component of a lower-limb robotic exoskeleton for integrating sensing capacity and enhancing multi-material direct additive manufacturing. IOP Conf Ser Mater Sci Eng 2021;1193(1):012097; doi: 10.1088/1757-899X/1193/1/012097.
13. Park JH, Jung HK, Lee JR. Development and evaluation of fall impact protection pads using additive manufacturing. Materials 2019;12(20); doi: 10.3390/ma12203440.
14. Hamzehei R, Kadkhodapour J, Anaraki AP, et al. Octagonal auxetic metamaterials with hyperelastic properties for large compressive deformation. Int J Mech Sci 2018;145:96–105; doi: 10.1016/j.ijmecsci.2018.06.040.
15. Nace SE, Tiernan J, Holland D, et al. A comparative analysis of the compression characteristics of a thermoplastic polyurethane 3D printed in four infill patterns for comfort applications. Rapid Prototyp J 2021;27(11):24–36; doi: 10.1108/RPJ-07-2020-0155.
16. Kechagias JD, Vidakis N, Petousis M. Parameter effects and process modeling of FFF-TPU mechanical response. Materials and Manufacturing Processes 2023;38(3):341–351; doi: 10.1080/10426914.2021.2001523.
17. Lin X, Coates P, Hebda M, et al. Experimental analysis of the tensile property of FFF-printed elastomers. Polym Test 2020;90:106687; doi: 10.1016/j.polymertesting.2020.106687.
18. Kalia K, Ameli A. Interfacial Bond Strength of Various Rigid/Soft Multi-Materials Printed via Fused Filament Fabrication Process. In: ASME 2020 Conference on Smart Materials, Adaptive Structures and Intelligent Systems American Society of Mechanical Engineers; 2020; doi: 10.1115/SMASIS2020-2298.
19. Lopes LR, Silva AF, Carneiro OS. Multi-material 3D printing: The relevance of materials affinity on the boundary interface performance. Addit Manuf 2018;23:45–52; doi: 10.1016/j.addma.2018.06.027.
20. Johnston R, Kazancı Z. Analysis of additively manufactured (3D printed) dual-material auxetic structures under compression. Addit Manuf 2021;38; doi: 10.1016/j.addma.2020.101783.
21. de León AS, Domínguez-Calvo A, Molina SI. Materials with enhanced adhesive properties based on acrylonitrile-butadiene-styrene (ABS)/thermoplastic polyurethane (TPU) blends for fused filament fabrication (FFF). Mater Des 2019;182; doi: 10.1016/j.matdes.2019.108044.
22. Hamidi A, Tadesse Y. Single step 3D printing of bioinspired structures via metal reinforced thermoplastic and highly stretchable elastomer. Compos Struct 2019;210:250–261; doi: 10.1016/j.compstruct.2018.11.019.
23. Dixit N, Jain PK. Effect of Fused Filament Fabrication Process Parameters on Compressive Strength of Thermoplastic Polyurethane and Polylactic Acid Lattice Structures. J Mater Eng Perform 2022;31(7):5973–5982; doi: 10.1007/s11665-022-06664-0.
24. García-Collado A, Blanco JM, Gupta MK, et al. Advances in polymers based Multi-Material Additive-Manufacturing Techniques: State-of-art review on properties and applications. Addit Manuf 2022;50:102577; doi: 10.1016/j.addma.2021.102577.
25. Mansouri MR, Montazerian H, Schmauder S, et al. 3D-printed multimaterial composites tailored for compliancy and strain recovery. Compos Struct 2018;184:11–17; doi: 10.1016/j.compstruct.2017.09.049.
26. Ngo TD, Kashani A, Imbalzano G, et al. Additive Manufacturing (3D Printing): A Review of Materials, Methods, Applications and Challenges. Compos B Eng 2018;143:172–196; doi: 10.1016/j.compositesb.2018.02.012.

27. Agrawal A, Choudhary A. Perspective: Materials informatics and big data: Realization of the “fourth paradigm” of science in materials science. APL Mater 2016;4(5); doi: 10.1063/1.4946894.
28. James G, Witten D, Hastie T, et al. An Introduction to Statistical Learning. Springer Texts in Statistics. Springer US: New York, NY; 2021.; doi: 10.1007/978-1-0716-1418-1.
29. Rajan K, Suh C, Mendez PF. Principal component analysis and dimensional analysis as materials informatics tools to reduce dimensionality in materials science and engineering. Statistical Analysis and Data Mining: The ASA Data Science Journal 2009;1(6):361–371; doi: 10.1002/sam.10031.
30. Popova E, Rodgers TM, Gong X, et al. Process-Structure Linkages Using a Data Science Approach: Application to Simulated Additive Manufacturing Data. Integr Mater Manuf Innov 2017;6(1):54–68; doi: 10.1007/s40192-017-0088-1.
31. D’Agostino D, Serani A, Campana EF, et al. Augmented Design-Space Exploration by Nonlinear Dimensionality Reduction Methods. 2019; pp. 154–165; doi: 10.1007/978-3-030-13709-0_13.
32. Berguin SH, Rancourt D, Mavris DN. Method to Facilitate High-Dimensional Design Space Exploration Using Computationally Expensive Analyses. In: AIAA Journal American Institute of Aeronautics and Astronautics Inc.; 2015; pp. 3752–3765; doi: 10.2514/1.J054035.
33. D’Agostino D, Serani A, Diez M. Design-space assessment and dimensionality reduction: An off-line method for shape reparameterization in simulation-based optimization. Ocean Engineering 2020;197; doi: 10.1016/j.oceaneng.2019.106852.
34. Bunnell S, Gorrell S, Salmon J, et al. Structural design space exploration using principal component analysis. J Comput Inf Sci Eng 2020;20(6); doi: 10.1115/1.4047428.
35. Bruère VM, Lion A, Holtmannspötter J, et al. Under-extrusion challenges for elastic filaments: the influence of moisture on additive manufacturing. Progress in Additive Manufacturing 2022;7(3):445–452; doi: 10.1007/s40964-022-00300-y.
36. Awasthi P, Banerjee SS. Fused Deposition Modeling of Thermoplastic Elastomeric Materials: Challenges and Opportunities. Addit Manuf 2021;46; doi: 10.1016/j.addma.2021.102177.
37. Anonymous. Essentium TPU 80A LF Technical Data Sheet. Pflugerville, TX; 2020.
38. Anonymous. Essentium TPU 74D Technical Data Sheet. Pflugerville, TX; 2020.
39. Logg A, Mardal K-A, Wells G, (eds). Automated Solution of Differential Equations by the Finite Element Method. Springer Berlin Heidelberg: Berlin, Heidelberg; 2012.; doi: 10.1007/978-3-642-23099-8.
40. Logg A, Wells GN. DOLFIN: a C++/Python Finite Element Library. ACM Transactions on Mathematical Software 2010;37(2):1–28; doi: 10.1145/1731022.1731030.
41. Geuzaine C, Remacle J. Gmsh: A 3-D finite element mesh generator with built-in pre- and post-processing facilities. Int J Numer Methods Eng 2009;79(11):1309–1331; doi: 10.1002/nme.2579.
42. Tawk C, Alici G. Finite element modeling in the design process of 3D printed pneumatic soft actuators and sensors. Robotics 2020;9(9); doi: 10.3390/ROBOTICS9030052.
43. Wang Y, Luo W, Huang J, et al. Simplification of Hyperelastic Constitutive Model and Finite Element Analysis of Thermoplastic Polyurethane Elastomers. Macromol Theory Simul 2020;29(4); doi: 10.1002/mats.202000009.
44. Yeoh OH. Hyperelastic material models for finite element analysis of rubber. Journal of Natural Rubber Research 1997;12:142–153.
45. Kandasamy K, Vysyaraju KR, Neiswanger W, et al. Tuning Hyperparameters without Grad Students: Scalable and Robust Bayesian Optimisation with Dragonfly. 2019.
46. Pedregosa F, Varoquaux G, Gramfort A, et al. Scikit-learn: Machine Learning in Python. 2012.